Geophysical Journal International

Geophys. J. Int. (2025) **243,** 1–15
Advance Access publication 2025 September 22
Research Paper

https://doi.org/10.1093/gji/ggaf376

Geologically guided ambient noise tomography inversion with 3-D interface structures: methodology and application to a gold mine region in China

Yujie Wang [1,2] Xin Wang,[1,2] Junliu Suwen,[1,2] Bao Deng [3] Qi-Fu Chen,[1,2] Tao Xu[2,4] and Zhongxing Wang[2,4]

[1] *Key Laboratory of Planetary Science and Frontier Technology, Institute of Geology and Geophysics, Chinese Academy of Sciences, Beijing* 100029*, China. E-mail: wangxin@mail.iggcas.ac.cn*
[2] *College of Earth and Planetary Sciences, University of Chinese Academy of Sciences, Beijing* 100049*, China*
[3] *School of Earth and Space Sciences, University of Science and Technology of China, Hefei* 230026*, China*
[4] *State Key Laboratory of Deep Petroleum Intelligent Exploration and Development, Institute of Geology and Geophysics, Chinese Academy of Sciences, Beijing* 100029*, China*

Accepted 2025 September 18. Received 2025 September 15; in original form 2025 March 5

SUMMARY

Seismic surface wave tomography, particularly when leveraging dense array data, has become a widely used method for investigating shallow subsurface velocity structures. The shallow structures are usually characterized by rapid seismic velocity changes (i.e. seismic interfaces) due to variations in rock properties, sedimentary environments or tectonic features. However, the commonly used grid-based parametrization of the velocity field in surface wave tomography often struggles to accurately constrain such interface geometries. In addition, traditional surface wave inversion methods typically rely on 1-D inversion at individual stations using dispersion curves, followed by interpolation to construct 2-D or 3-D models. This approach can sometimes introduce spurious features and reduce model reliability. To address these limitations, we propose a geological and level-set parametrization approach for surface wave tomography, allowing for the explicit consideration of interface structures in inversion. This method is then combined with the Ensemble Kalman Inversion to optimize subsurface structures. Synthetic tests demonstrate that integrating 3-D interface parametrization in tomography significantly enhances the reliability of the velocity model and the recovery of interface geometries. Applying this approach to the Woxi gold mine region in China yielded inversion results that closely align with existing borehole data. This study highlights the advantages of level-set parametrization for 3-D interface imaging in seismic tomography, underscoring its potential in subsurface mineral exploration.

Key words: Inverse theory; Tomography; Surface waves and free oscillations.

1 INTRODUCTION

Seismic tomography is a fundamental method for investigating Earth's subsurface structure (Aki *et al.* 1977; Dziewonski *et al.* 1977; Romanowicz 2012). Its implementation involves key components: model parametrization, forward modelling, inversion and regularization (Aki *et al.* 1977). Model parametrization plays a critical role, providing the quantitative framework for describing the subsurface medium and underpinning subsequent modelling efforts. Diverse parametrization approaches exist, from uniform grids to adaptive non-uniform schemes (Aki & Lee 1976; Sambridge *et al.* 1995; Rawlinson & Houseman 2010; Fang *et al.* 2019). However, the seismic tomography inverse problem is inherently underdetermined. As a result, the choice of parametrization strongly impacts the uniqueness and accuracy of solutions, often leading to variations in tomography results. To mitigate this, incorporating geological information, such as known structural interfaces or expected velocity ranges of specific geological units, into the inversion can help narrow model space uncertainty and enable the derivation of geologically meaningful models from the mathematically permissible set (Tarantola 2005; Tso *et al.* 2021).

Earth's interior contains seismic discontinuities at various scales, including global-scale features and localized velocity contrasts (Dziewonski & Anderson 1981; Shearer 1991; Yuan *et al.* 1997; Li *et al.* 2008; Wang & Niu 2011; Zheng *et al.* 2015). Conventional parametrization, primarily describing smoothly varying velocity fields, struggles to capture these sharp contrasts (Fig. 1b). In addition, regularization techniques applied in tomography

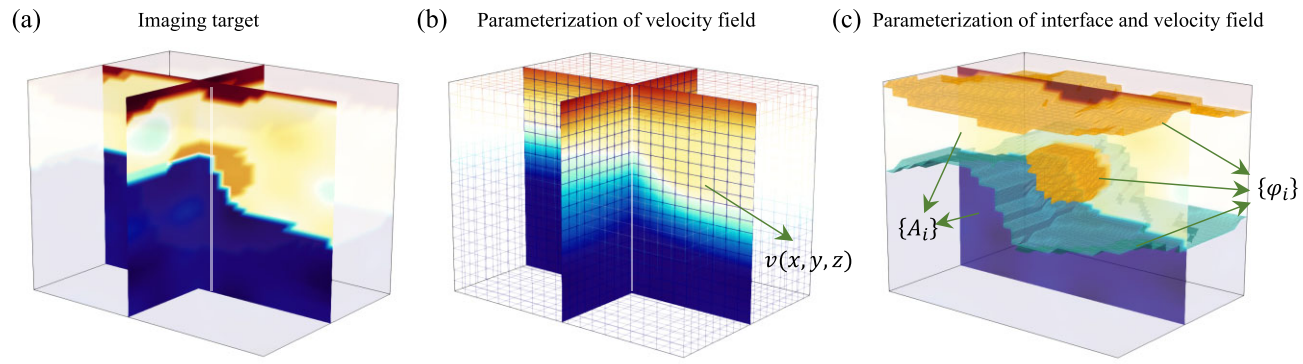

Figure 1. Illustration of the imaging setup, including the input 3-D velocity model and potential results from different parametrization strategies. (a) The input 3-D velocity model, with two interfaces and a low-velocity body. (b) Potential imaging result using traditional parametrization. Traditional seismic tomography typically employs uniform grids, where $v(x, y, z)$ represents the velocity values within each cell. Regularization enhances numerical stability but compromises the accurate reconstruction of abrupt velocity changes. (c) Possible imaging result using 3-D interface parametrization. In this method, $\{\varphi_i\}$ represents the level-set equations controlling the interfaces, and $\{A_i\}$ represents the equations controlling the velocity field.

inversion often suppress velocity contrasts across discontinuities (Worthen *et al.* 2014; Muir *et al.* 2022; Tsai *et al.* 2023), improving numerical stability but at the expense of accurately reconstructing abrupt velocity changes. Even when using dense grids and moderate smoothing, conventional parametrization frequently introduces artefacts that contradict physical expectations (Lin *et al.* 2014; Hosseini *et al.* 2019). To overcome these limitations, incorporating interface-specific constraints directly into the inversion framework is essential for accurate subsurface reconstructions. This allows for the simultaneous optimization of seismic velocity fields and interface geometries, leading to more accurate reconstructions of subsurface structures (Muir & Tsai 2020; Tsai *et al.* 2023).

The level-set method effectively describes and reconstructs interfaces by modelling their evolution with a globally defined continuous function (Osher & Sethian 1988). It has been widely applied in various fields, including hydraulic reservoir modelling (Iglesias 2015; Chada *et al.* 2018), electrical impedance tomography (Chada *et al.* 2018), interwell seismic tomography, gravity and magnetic exploration (Zheglova *et al.* 2012, 2018; Li *et al.* 2014, 2017; Isakov *et al.* 2015; Lu & Qian 2015; Li & Qian 2016) and machine learning (Kovachki & Stuart 2019). In seismology, early applications like Zheglova *et al.* (2012) reconstructed 2-D subsurface interfaces with distinct discontinuities. Subsequently, Muir & Tsai (2020) proposed a geometric and level-set-based Ensemble Kalman Inversion (EKI) framework for seismic traveltime tomography, constraining shallow velocity structures with interfaces under the assumption of a uniform seismic velocity field between interfaces. This framework has been applied to refine the basin basement in the Los Angeles Basin (Muir *et al.* 2022) and to image near-surface structures in Ridgecrest, California (Yang *et al.* 2021). However, these previous studies primarily focused on 2-D linear array data and often assumed uniform seismic velocities between interfaces, limiting flexibility for depth-varying properties. Moreover, they only focused on layered boundaries (Muir & Tsai 2020; Yang *et al.* 2021; Muir *et al.* 2022), overlooking more complex geological concepts such as fault attributes or internal heterogeneities. Incorporating these geological structures into seismic inversion through a geology-driven parametrization facilitates reconstructions that align more closely with geological knowledge (Tsai *et al.* 2023). This explicit integration of geological models represents an evolving and crucial direction in seismic tomography studies. By utilizing more relevant prior information, this approach significantly improves subsurface constraints, enhancing model plausibility and geological understanding (Tsai *et al.* 2023).

Ambient noise tomography (ANT) is widely used for subsurface 3-D structures imaging (e.g. Yao *et al.* 2006; Lin *et al.* 2008,2013; Yao *et al.* 2010; Fang *et al.* 2015; Chmiel *et al.* 2019; Du *et al.* 2020). Traditional ambient noise tomography typically involves two steps: first deriving 2-D velocity maps, then inverting dispersion curves for 1-D *S*-wave velocity models (Montagner & Jobert 1988; Ritzwoller & Levshin 1998; Barmin *et al.* 2001). While a proposed one-step surface wave tomography method directly derives 3-D velocity models from dispersion curves, the two-step approach remains more common, especially for joint inversion integrating additional seismic data (Feng & An 2010; Fang *et al.* 2015). A major limitation of the two-step approach is that each location's velocity structure inversion is treated independently, without incorporating lateral constraints. This limitation, combined with noise and inversion non-uniqueness, often introduces artefacts in the final results (Ritzwoller & Levshin 1998; Barmin *et al.* 2001; Boschi & Ekström 2002; Fang *et al.* 2015). The level-set method offers a promising solution by parametrizing interfaces, enhancing lateral constraints and reducing artefacts. However, its application in passive source seismic imaging has not been widely adopted (Muir & Tsai 2020).

In this study, we extend the previous level-set parametrization (Muir & Tsai 2020) by adopting a geological and level-set approach for ambient noise seismic tomography. This framework models 3-D layered, heterogeneous and fault-included interfaces, along with non-uniform velocity fields. Incorporating EKI, we outline its principles, demonstrate advantages through numerical simulations and apply it to dense array data from the Woxi gold mine region to evaluate practicality and stability for subsurface mineral exploration.

2 METHODOLOGY

The geological and level-set parametrization approach integrates interface perturbations, velocity fields and geological structures into a velocity model using Gaussian Random Fields (GRFs; Osher & Sethian 1988; Ritzwoller & Levshin 1998; Gibou *et al.* 2018), following the framework introduced by Muir *et al.* (2022). This

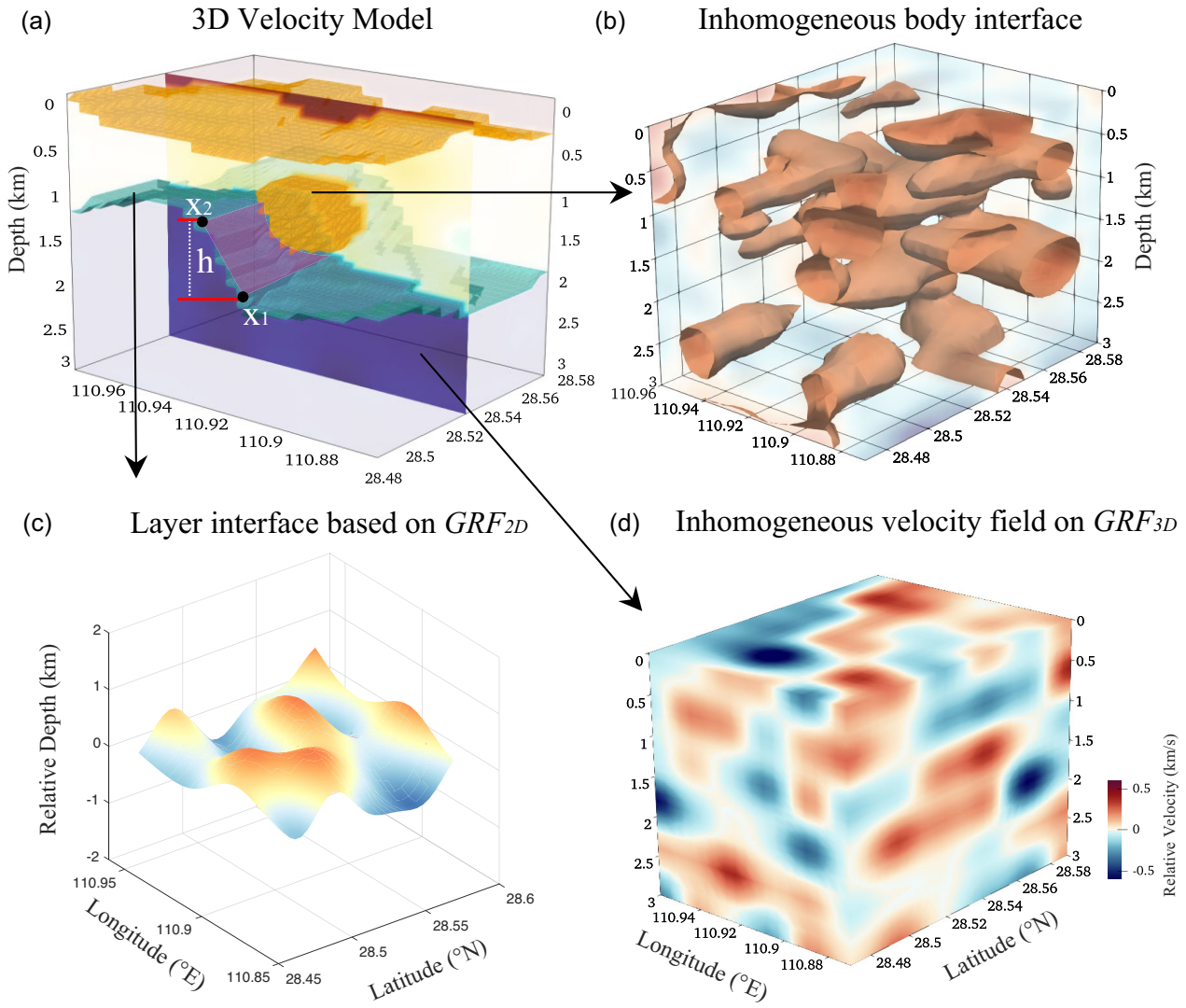

Figure 2. Methods used to represent a 3-D velocity model using combinations of GRFs. (a) The combined velocity model, where stratigraphic interfaces and closed surfaces are represented by isolines. Parameters x_1, x_2 and h are used to model a simple fault cutting through the interfaces. (b) The inhomogeneous bodies are defined using the level set equation, based on zero-level isosurface the 3-D GRF. (c) The velocity interfaces are defined using 2-D GRFs. Here, depth values depict interface perturbations from an average depth, which is an inversion parameter. (d) The velocity field is defined using a 3-D GRF. Similarly, velocity values represent perturbations around a mean velocity, also an inversion parameter.

approach is similar to the spatial damping and smoothing techniques used in the commonly applied Tikhonov regularization framework (Aster *et al.* 2018). In our implementation, 2-D GRFs are utilized to generate $\{\varphi_i\}_{i=1}^{n}$, where n represents the total number of interfaces, and φ_i defines the i-th velocity discontinuity (Fig. 2c). Similarly, 3-D GRFs are used to generate $\{A_i\}_{i=1}^{n}$, where A_i defines the velocity field between these discontinuities (Fig. 2d). While our approach builds on Muir *et al.* (2022), it extends their method into 3-D and explicitly incorporates inhomogeneous body boundary descriptions. Fig. 2 shows that 3-D level-sets can effectively represent arbitrarily shaped layers and inclusions, depicting the zero-level isosurface of a 3-D GRF. In addition, this study utilizes multiple level sets, enabling the inversion to capture not only a single inhomogeneous body but also multiple interconnected inhomogeneous structures.

To generate the GRFs, we utilize both 2-D and 3-D anisotropic covariance functions, $C_{2-\mathrm{D}}(x, y)$ and $C_{3-\mathrm{D}}(x, y)$, respectively (Rasmussen & Williams 2005). The expression for $C_{2-\mathrm{D}}(x, y)$ is given as:

$$C_{2-\mathrm{D}}(x, y) = \sigma_b \exp\left(-(x-y)^{\mathrm{T}} \begin{bmatrix} \frac{1}{l_b x^2} & 0 \\ 0 & \frac{1}{l_b y^2} \end{bmatrix} (x-y)\right), \quad (1)$$

where x and y represent the position vectors. $l_b x$ and $l_b y$ denote characteristic lengths of horizontal boundary perturbations, representing their spatial correlation; and σ_b characterizes boundary perturbation magnitude along depth. The $C_{3-\mathrm{D}}(x, y)$ is expressed as:

$$C_{3-\mathrm{D}}(x, y) = \sigma_v \exp\left(-(x-y)^{\mathrm{T}} \begin{bmatrix} \frac{1}{l_v z^2} & 0 & 0 \\ 0 & \frac{1}{l_v x^2} & 0 \\ 0 & 0 & \frac{1}{l_v y^2} \end{bmatrix} (x-y)\right), \quad (2)$$

where $l_v x, l_v y$ and $l_v z$ represent the characteristic lengths of the 3-D velocity field, while σ_v quantifies the magnitude of velocity perturbations. The covariance functions are transformed into GRFs within the defined Cartesian coordinate system through

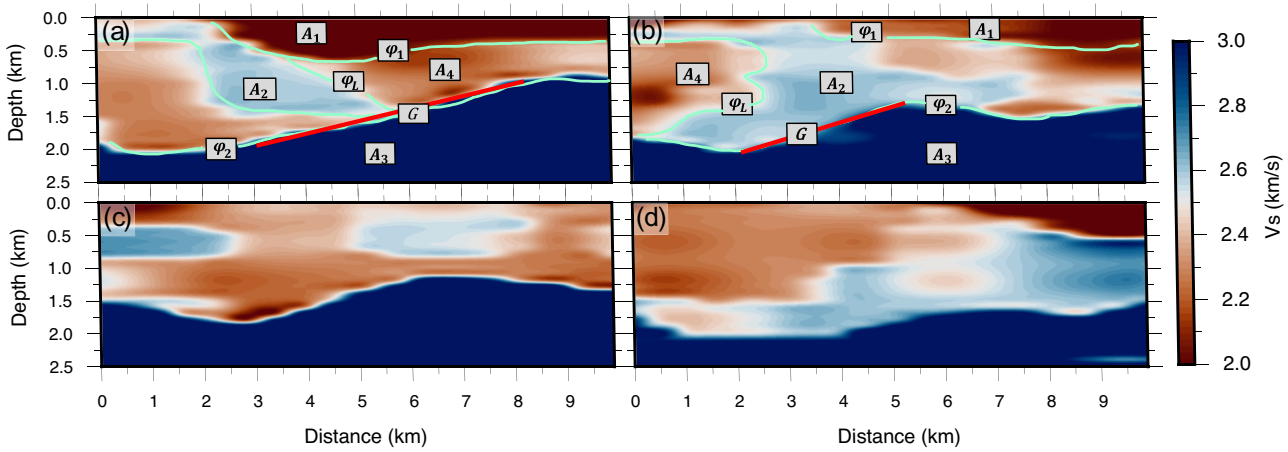

Figure 3. Cross-sections of stochastic models generated using geological and level-set parametrization. (a) and (b) show representative stochastic models, fully annotated to illustrate the parametrization. These include 2-D GRFs defining boundaries $\{\varphi_{1,2}\}$, 3-D GRFs defining velocity fields $\{A_{1,2,3,4}\}$, the inhomogeneous body defined by a 3-D level-set equation $\{\varphi_L\}$, and a simple fault structure {G} controlled by geometric parameters $\{x_1, x_2, h\}$. (c) and (d) present additional stochastic realizations of the models generated during inversion, emphasizing the inherent randomness and variability captured by the GRFs-based parametrization.

the Karhunen-Loève expansion (Béreš 2018). For computational efficiency with high-dimensional data, the Nyström method approximates the eigen-decomposition of the covariance matrix, significantly reducing computational burden for large-scale samples (Nyström 1930).

Prior geological knowledge (e.g. layered media, faults, inhomogeneities) crucially informs the geological parameter vector {G} (Tsai *et al.* 2023). GRFs' mean values define stratigraphic interface depths and average velocity fields. Fault characteristics, like discontinuity points x_1, x_2 along the y-axis and vertical slip h (Fig. 2a), also contribute. The general model parameter vector is $u = [\{\varphi_i\}_{i=1}^n, \{A_i\}_{i=1}^n, \{\mathrm{G}\}]$. To provide a visual example of the models that can be constructed with this approach, we present an example in Fig. 3. The model consists of three key features: two velocity boundaries, a fault and an inhomogeneous body. These features are parametrized by the fault geometry, described by parameters $\{x_1, x_2, h\}$, and the boundary of the inhomogeneous body, defined by a 3-D level-set function $\{\varphi_L\}$. In this specific case, the model parameter vector is $u = [\{\varphi_i\}_{i=1}^2, \{A_i\}_{i=1}^4, \varphi_L, \{x_1, x_2, h\}$. The velocity model $F(u)$ is obtained by concatenating and deforming these components (Fig. 3).

The forward modelling framework in this study involves constructing the model parameter vector u, building the velocity model $\mathrm{F}(u)$ and computing the forward response $\mathrm{H}(\mathrm{F}(u))$(Muir & Tsai 2020). The forward mapping G can thus be expressed as $G(u) = \mathrm{H}(\mathrm{F}(u))$. We implement this using the Surf96 program, which considers the *S*-wave velocity structure beneath each station (Herrmann 2013). In our approach, the inversion goal is not the velocity model $\mathrm{F}(u)$, but rather the model parameter vector u. The inversion process is an optimization of the model parameter vector. The resulting optimal u^* contains refined interface and velocity field information, providing a clear representation when mapped to the Cartesian coordinate system $(\mathrm{F}(u^*))$.

This study employs a parallelized EKI strategy (Evensen 2012; Iglesias 2016). This algorithm is chosen for several key advantages: (1) ensemble member independence enables parallel computation for efficiency; (2) absence of derivatives allows solving large-scale nonlinear or black-box inverse problems (Iglesias 2016) and (3) Low-rank approximation and the Woodbury matrix identity further reduce memory costs for updating covariance matrices, facilitating efficient large data set processing. These advantages make EKI well-suited to our parametrization framework.

Combining level-set parametrization with EKI transforms the geophysical inverse problem into an optimization problem for the model. The invariant structure of the model parameter vector ensures that interface structures of interest can be constrained and optimized. However, applying this parametrization requires strong prior information to avoid false structures. Nevertheless, practice and research suggest that EKI with appropriate coarse parametrization is an effective inversion tool (Tso *et al.* 2021). A flowchart of this framework, illustrated with background noise tomography, is provided in Fig. 4.

3 SYNTHETIC TEST

To evaluate the feasibility of combining the level set method with EKI in ambient noise tomography, we first performed synthetic tests. A 3-D shear wave velocity model was constructed featuring two interfaces, a fault structure and an ellipsoidal low-velocity anomaly (Figs 5a and e). The average shear wave velocities of the three layers, from top to bottom, are 2.0, 2.8 and 3.3 km s^{-1}, respectively. Velocity perturbations were also introduced within each layer instead of assuming a uniform velocity field. The ellipsoidal low-velocity anomaly is located within the second layer and has an average velocity of 2.5 km s^{-1}. Seismic stations are located on the surface, consistent with the actual station distribution used in the real data, as described in Section 4. Using this velocity model, we computed synthetic Rayleigh wave phase velocity dispersion curves with the Surf96 program (Herrmann 2013), considering the *S*-wave velocity structure beneath each station. The frequency bands of the synthetic dispersion curves range from 0.2 to 1.8 s, corresponding to the observed dispersion data shown in Section 4.

The inversion framework employed in this study is a geologically guided optimization procedure. Prior to the inversion process, a preliminary understanding of the subsurface medium is typically established using existing geological information or results from initial inversion. This prior knowledge is then characterized and

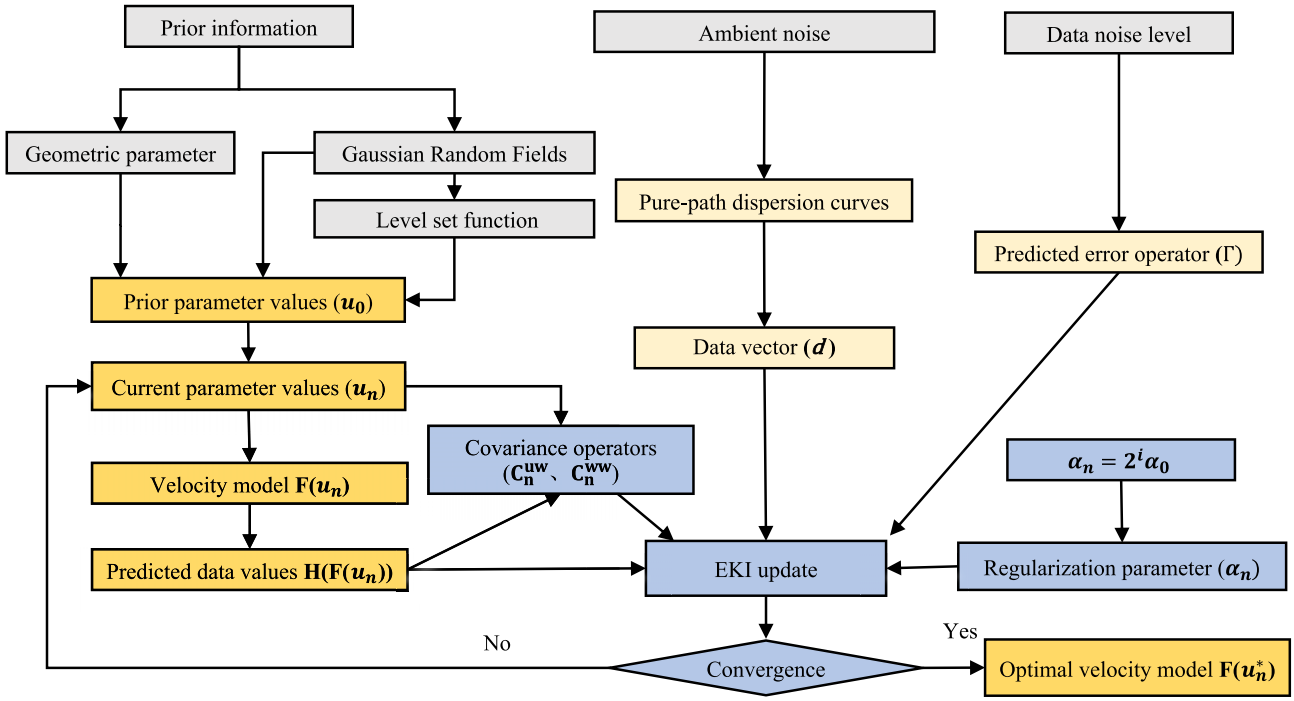

Figure 4. A flow chart illustrating the EKI inversion process. Grey modules represent prior information and data sources, light yellow modules represent data, orange modules represent model parameters and responses and blue modules represent the EKI iteration process. Key notations in this framework include: u_0 (prior model parameter vector), u_n (current model parameter vector at iteration n), F(u_n) (velocity model at iteration n), d (data vector), H(F(u_n)) (forward predicted data values), C_n^{uw} and C_n^{ww} (covariance operators), α_0 (initial regularization parameter), α_n (regularization parameter), Γ (predicted error operator) and F(u_n^*) (optimal velocity model upon convergence) Technical details related to the EKI can be found in Iglesias (2016) and Muir & Tsai (2020).

incorporated into the inversion workflow, enabling the refinement and exploration of geological features of interest. To evaluate the influence of prior information on the inversion results, different assumptions about the subsurface structure were tested. These assumptions include the following: (1) incorporating only two velocity boundaries (Fig. 5b), (2) two velocity boundaries and fault structures (Fig. 5c) and (3) two velocity boundaries, fault structures and a 3-D level set equation (Fig. 5d). The model construction for case (3) is the same as the example shown in Section 2. However, cases (1) and (2) lack the corresponding types of prior information. Synthetic tests show that inversion results are closely related to the type of prior information introduced. However, they are not dependent on specific values, such as layer depths or GRFs characteristic values. In practical inversion studies, it is sufficient to conduct a preliminary survey of the study area or estimate these parameter values based on initial inversion results. In this study, we employed an ensemble of 200 randomly initialized models in the EKI inversion to ensure the stability of the inversion results (Iglesias 2016).

Figs 5(a)–(d) provide an intuitive visualization of how different prior information influences inversion results, illustrated through contour maps. To further explore the finer details of these results, a 2-D profile is presented in Figs 5(e)–(h). Initially, without explicit prior information, a traditional inversion using the linear iterative Surf96 program (Herrmann 2013) provided insights into the approximate velocity structure (Fig. 6a). This approach independently inverts dispersion curves beneath each station for 1-D *S*-wave velocity profiles (hereafter we refer to this as the 1-D inversion method). For this, an initial model derived from the synthetic model's average velocity was adopted. The maximum inversion depth was consistently set at 3 km. To minimize the impact of model layering, both the layer count and thicknesses were kept consistent with our subsequent level-set method, with layers gradually thickening from 0.1 to 0.2 km. This inversion is carried out using a linearized iterative solver that minimizes weighted residuals between observed and predicted data, with smoothness constraints applied Tikhonov regularization. The resulting models (Fig. 6c) successfully capture key subsurface features, such as the shallow low-velocity layer and the low-velocity body. However, the boundaries of the fault structure, as well as the location and magnitude of the low-velocity body, remain unclear.

From the results of this 1-D inversion, two velocity discontinuities can be inferred at average depths of approximately 0.25 and 1.25 km. By incorporating these velocity discontinuities into the level-set inversion, we achieved better-constrained subsurface structures (Figs 5b and f). In this updated result, the shallow low-velocity layer, the low-velocity body and the velocity discontinuities are more distinct, with a fault structure likely present in the middle of the profile. To further refine the fault structure, simple geometric parameters for the fault structure were introduced, including its location and vertical displacement. While more complex mathematical models and additional parameters could enhance the representation of fault structures, further investigation is needed. Nevertheless, incorporating these fault parameters made it possible to resolve the fault structure in the inversion results (Figs 5c and g). Further analysis suggests the possible existence of a low-velocity body at depths ranging from 1 to 1.5 km. If the velocity contrast between the low-velocity body and the surrounding medium is substantial, its boundary can be modelled using the level set equation. By incorporating the inhomogeneous body interface into the inversion (Figs 5d

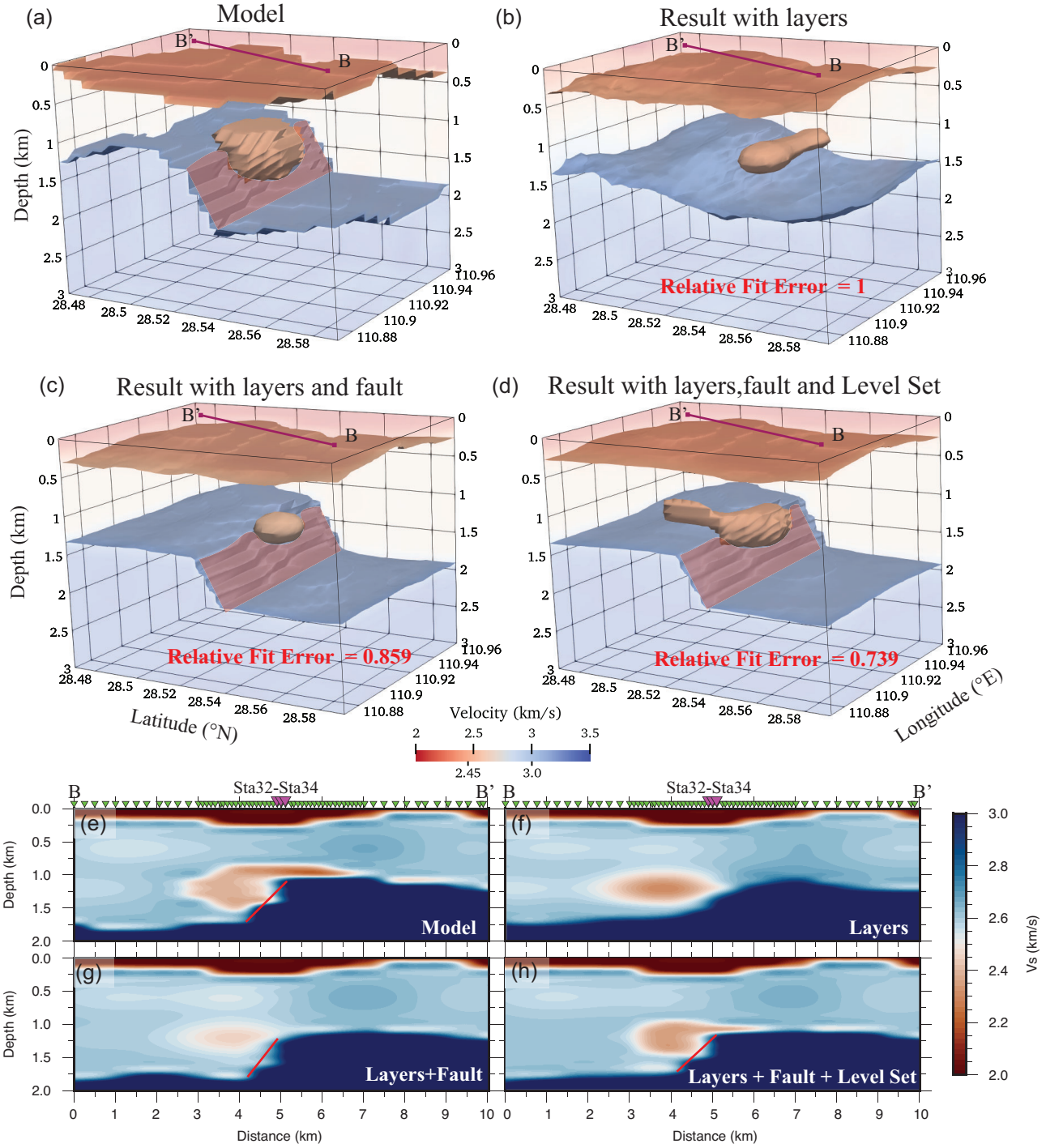

Figure 5. The influence of different prior information on inversion results. (a) The *S*-wave velocity model used to generate the synthetic data. (b) Inversion results incorporating prior information of two velocity interfaces. (c) Inversion results incorporating prior information about two velocity interfaces and fault parameters. (d) Inversion results further incorporating a 3-D zero-level set surface. The relative fit error quantifies improvement in data fit, calculated as the ratio of the current model's residual L2-norm to that of the baseline two-layer model (Fig. 5b). (e), (f), (g) and (h) show 2-D cross-sections corresponding to (a), (b), (c) and (d), respectively. In subfigures (e) and (g), the red line indicates the fault structure. The distribution of seismic stations and the locations of profiles are shown in Fig. 8.

and h), the resulting velocity model shows better consistency with the input model.

Our geology-driven parametrization is directly informed by incorporated prior geological knowledge. Synthetic tests demonstrate that integrating specific priors (e.g. layer numbers, fault characteristics) refines structural constraints (Fig. 5). While our examples use simplified faults, the framework accommodates greater complexity, potentially via tools like GemPy (de la Varga *et al.*

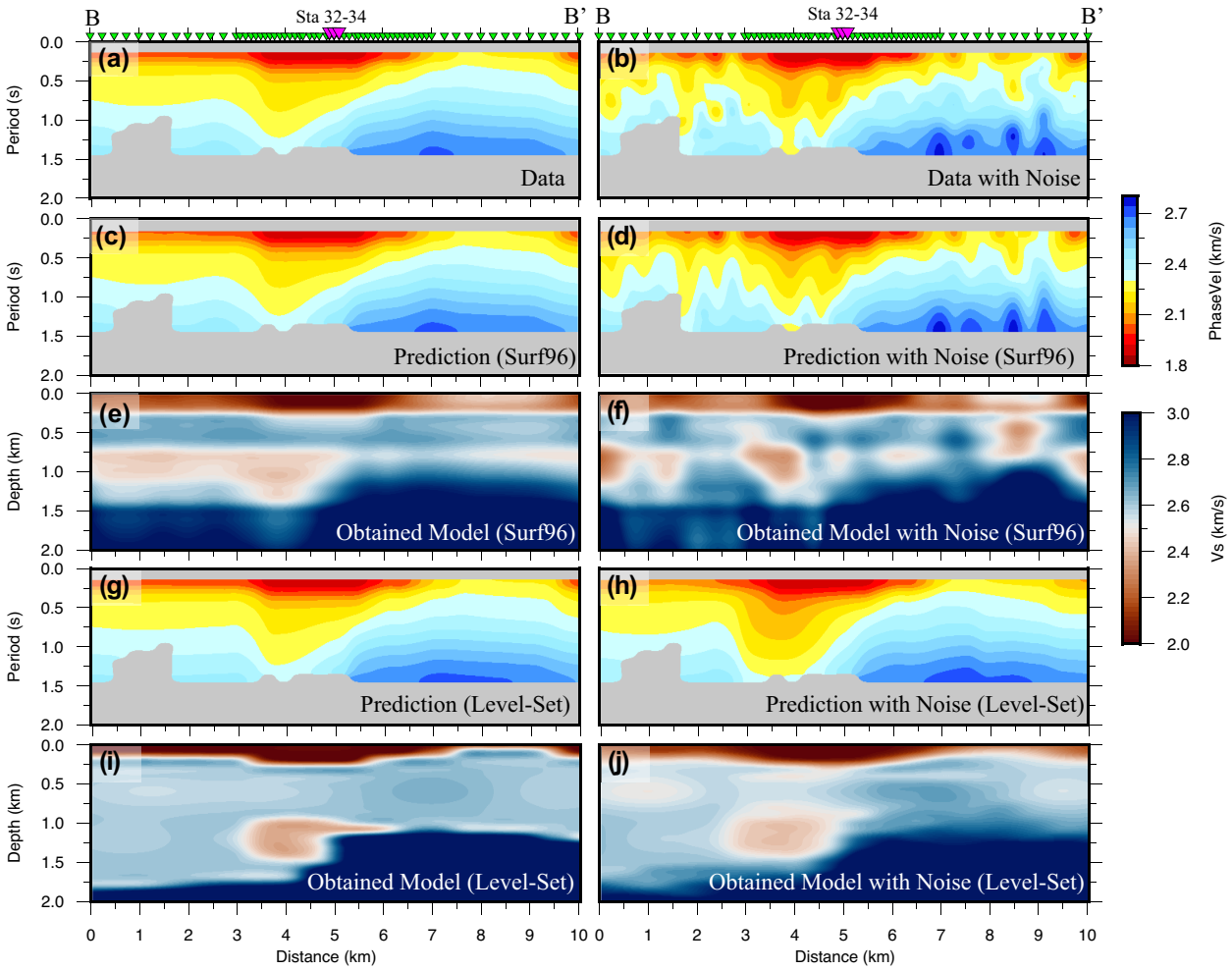

Figure 6. Comparison of inversion results for the L3 profile (BB') using noise-free and noisy synthetic data. Locations are shown in Figs 5(a) and 8. (a) Dispersion curves for synthetic data without noise. Green triangles indicating the locations of seismic stations, and the purple triangles mark the stations used for displaying the velocity profiles shown in Fig. 7. (b) Dispersion curves for synthetic data with noise. (c) Predicted dispersion curves from the 1-D Surf96 inversion using noise-free data. (d) Predicted dispersion curves from the 1-D Surf96 inversion using noisy data. (e) The velocity model obtained using the 1-D Surf96 inversion with noise-free data. (f) Similar to (e), but for the inversion with noisy data. (g) Predicted dispersion curves from the level-set method using noise-free data. (h) Predicted dispersion curves from the level-set method using noisy data. (i) The velocity model obtained using the level-set method with noise-free data. (j) Similar to (i), but for the inversion with noisy data.

2019). Non-uniqueness is best mitigated by quality data and robust priors; simpler parametrizations suit contexts with sparse prior knowledge (Cipta *et al.* 2018; Tsai *et al.* 2023). The suitability of priors can be practically assessed via data misfit analysis (e.g. Relative Fit Error shown in our synthetic tests, Fig. 5) and geological judgment. Our study demonstrates that this level-set based interface parametrization, guided by such priors, yields more detailed and geologically interpretable interface models compared to conventional tomography reliant primarily on generalized smoothness constraints, thereby facilitating subsequent geological analysis.

To simulate real-world conditions during inversion with noisy data, tests were conducted using different methods on data sets containing noise (Fig. 6). This simplified noise model was designed to approximate specific false perturbations observed in real dispersion curves extracted from field data. Gaussian random noise was added to the dispersion curves as input for the inversion. After adding noise, the dispersion curves show strong local variations (Fig. 6b), which is a common issue in real data processing. In contrast, our synthetic tests show that complex geological features, such as faults and inhomogeneous bodies, produce smooth dispersion curves (Fig. 6a), confirming that such sharp fluctuations are primarily caused by incoherent noise.

The imaging results obtained from the array-based interface parametrization remained largely unchanged, whereas the 1-D inversion approach exhibited significant discrepancies (Fig. 6). Specifically, the results from the single-station method (Figs 6c–f) show a tendency to overfit the noise, producing spurious features that lack clear geological meaning. In contrast, the results from the level-set method, which are based on array-data processing and continuous medium parametrization (Figs 6g–j), effectively mitigate the influence of noise. This is because, in 1-D inversion, the *S*-wave velocity

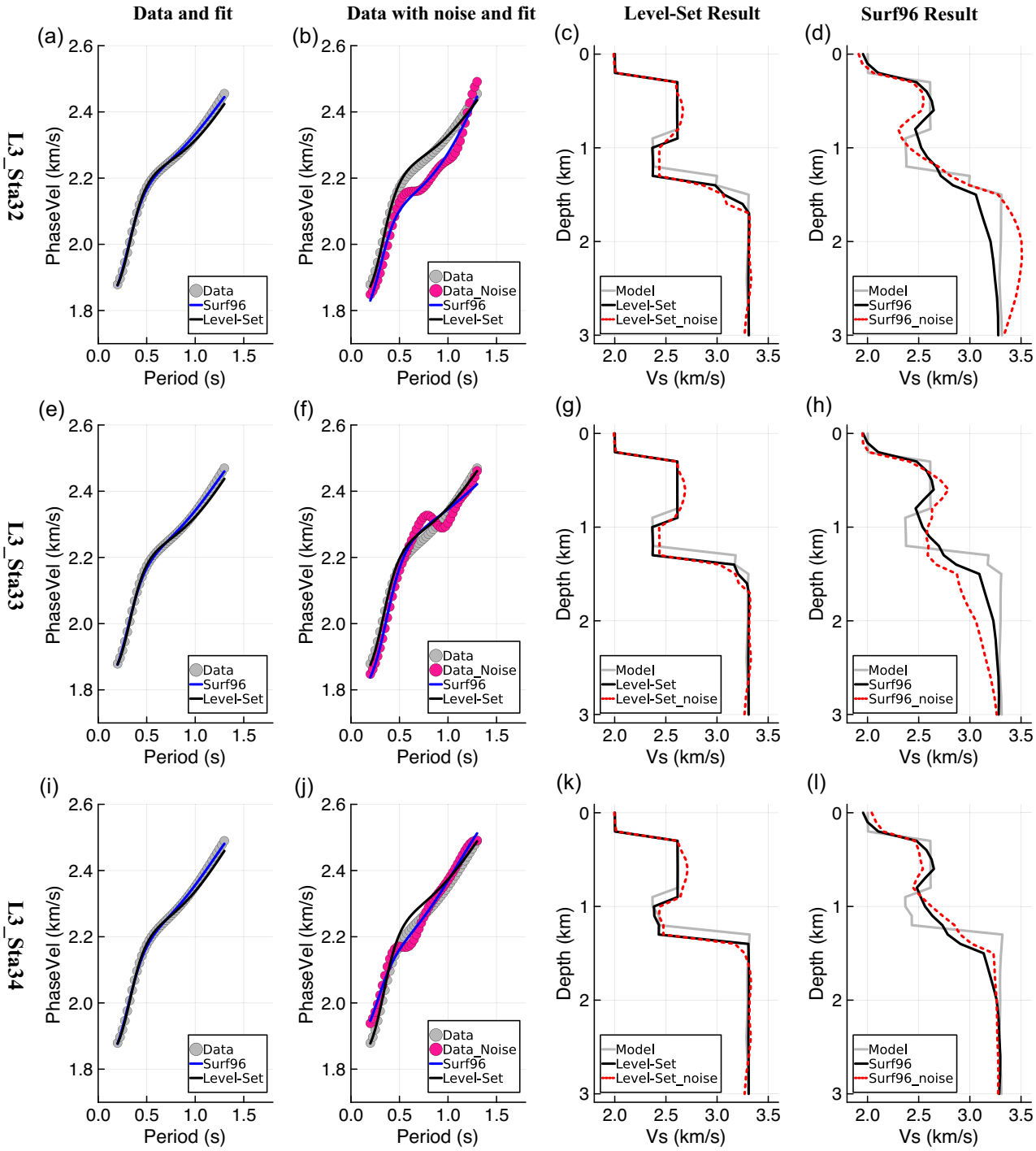

Figure 7. Comparison of data fitting and the obtained velocity models for stations 32–34 (station spacing ∼100 m) along the L3 line using different methods. (a) Data fitting for station 32 without considering noise in the synthetic test. (b) Similar to (a), but with noise included in the data. (c) Velocity models obtained using the level set method. (d) Velocity models obtained using the 1-D inversion method. (e–l) Similar to (a–d), but for stations 33 and 34.

structure beneath each station is inverted independently, without lateral constraints between neighbouring stations. Consequently, the inherent non-uniqueness of the nonlinear inversion process can introduce artefacts into the final 2-D/3-D models. In contrast, the level-set method, by leveraging array data and its intrinsic ability to produce laterally coherent and continuous velocity structures through GRFs and level-set functions, effectively imposes mutual constraints between neighbouring stations. This inherent continuity helps mitigate the impact of random noise on the inversion results. Even with noisy data, the level set method accurately recovered the input model (Fig. 6j), highlighting its stability and reliability.

Fig. 7 illustrates 1-D velocity models and dispersion curve fits for three stations along the central section of the L3 line (Fig. 8).

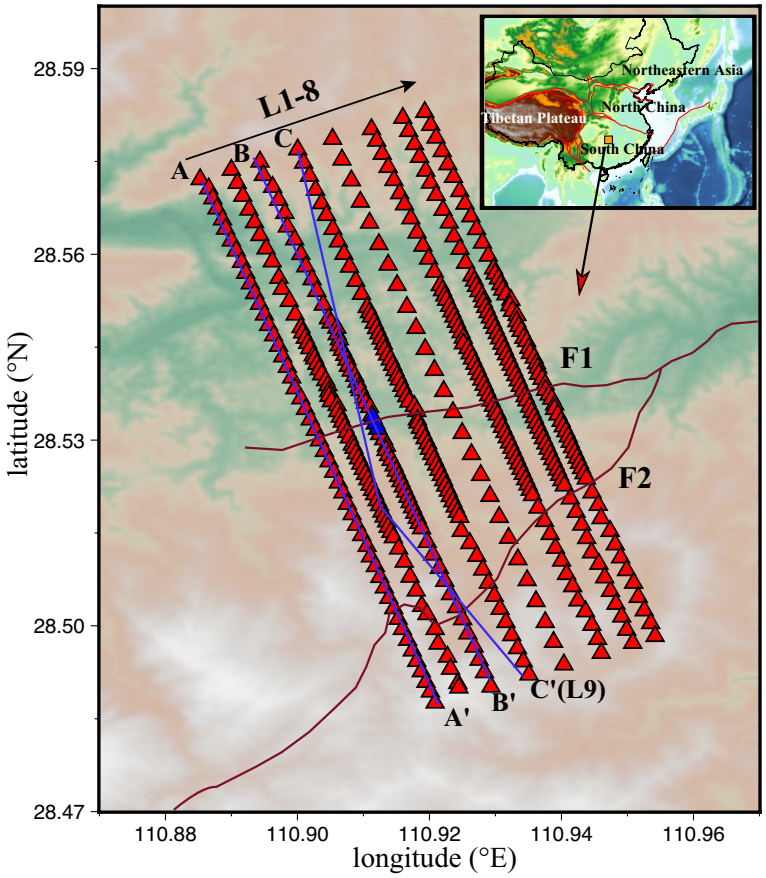

Figure 8. Seismic array layout and regional geological context of the Woxi gold mine study area. The triangles represent the seismic stations, and the red lines indicate mapped faults. F1 and F2 denote major regional faults (Li *et al.* 2022). The blue lines represent the locations of AA', BB' and CC' profiles. The upper right panel provides the broader geological context of the region, with red lines represent the major boundaries between different tectonic blocks (Wessel *et al.* 2019).

In the absence of noise, all models reasonably fit the input dispersion curves (Figs 7a, e and i). However, the resulting velocity models differ significantly, highlighting the non-uniqueness of inversion and the limitations of dispersion curves alone in constraining subsurface structures. The velocity structure derived using the array-based interface parametrization method closely matches the input model, effectively capturing both the depth and magnitude of velocity changes at discontinuities. In contrast, the traditional 1-D inversion method, while able to reflect overall velocity trends, fails to accurately constrain the interface locations due to its tendency toward smooth velocity variations (Figs 7d, h and l). When noise is introduced, perturbations appear in the dispersion curves between adjacent stations (Figs 7b, f and j). The array-based level set method leverages array data to suppress the noise and is able to recover the 1-D velocity structure beneath each station (Figs 7c, g and k). In contrast, the traditional 1-D inversion method shows substantial discrepancies in the velocity models obtained beneath adjacent stations (Figs 7d, h and l). These analyses further highlight the stability of the level-set inversion.

The synthetic tests also reveal that even when the dispersion data show high fitting accuracy, substantial discrepancies can still occur in the obtained velocity models. This highlights the need for additional information to better constrain the subsurface structure. On one hand, a single data set has limited ability to constrain the structure, and relying solely on surface wave dispersion data to define interfaces is inadequate. A straightforward way to address this limitation is to incorporate additional data sets for joint inversion. On the other hand, introducing inherent interfaces as prior information and constraining their variations can significantly enhance the realism of the imaging results. This approach offers a flexible framework for integrating interface information into the inversion process.

4 APPLICATION TO THE WOXI GOLD MINE

4.1 Geological background and station distribution

We apply our method to dense array data from the Woxi gold mine in Hunan, China, to assess its practicality (Fig. 8). Situated in the central Xuefeng arcuate structural belt of the Jiangnan Ancient Land Gold Metallogenic Belt, the mine is a key site for Au-Sb-W deposits (Peng *et al.* 2003) and hosts a large-scale co-occurrence of these minerals (Li *et al.* 2022). The geological information for this region was primarily obtained through a combination of geological mapping (Kuang *et al.* 2004; Shen & Liu 2017) and borehole data (Dai *et al.* 2022), with the borehole locations shown in Fig. 10. The exposed lithologies in the region, from oldest to youngest, include the Lengjiaxi Group, the Banxi Group and Cretaceous formations. The Lengjiaxi Group primarily consists of grey-green slates, with intercalated quartzites and sandstones, unconformably overlaid by the Banxi Group, which is the most extensive formation in the area.

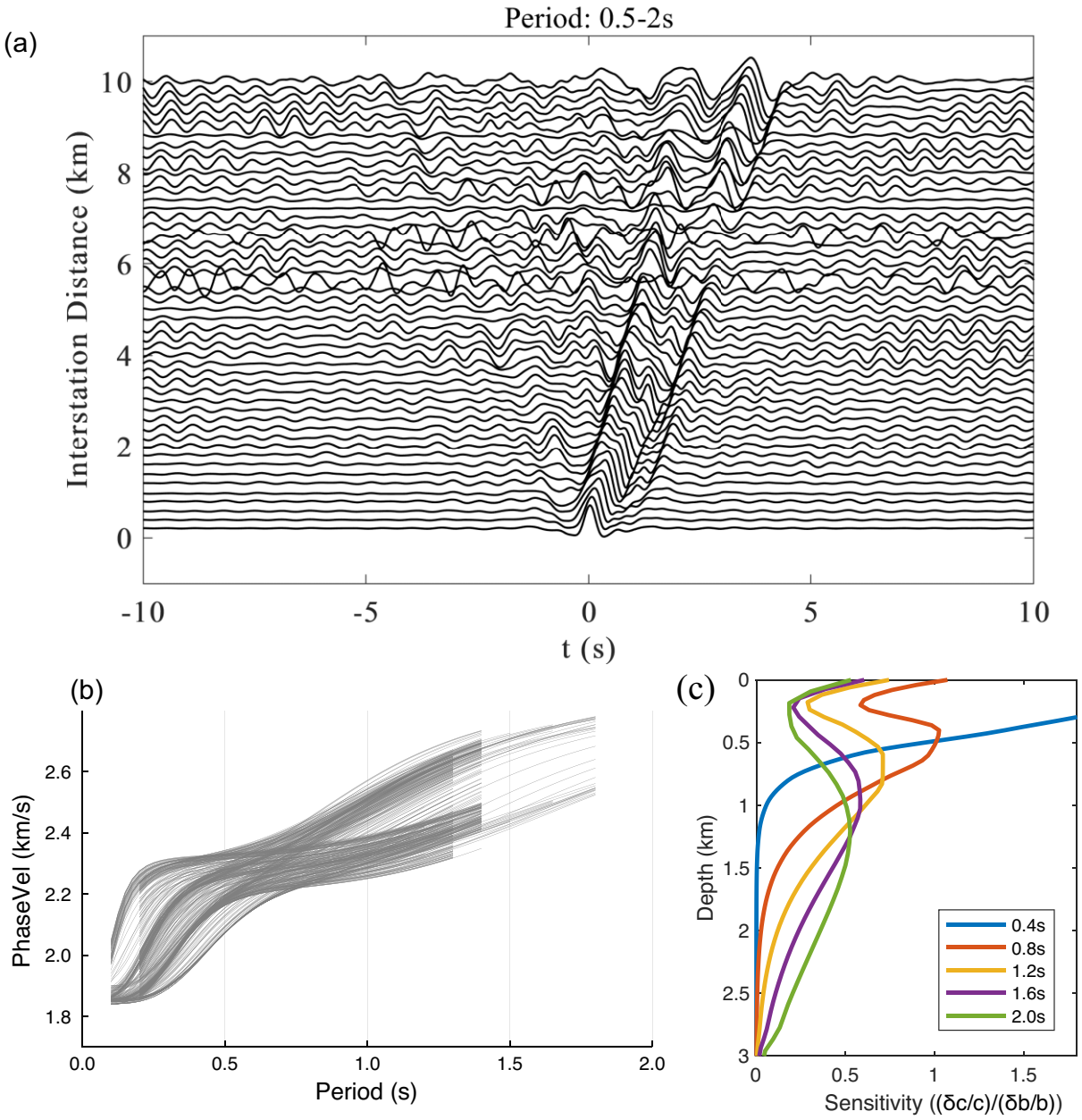

Figure 9. Data characteristics for the Woxi gold mine study. (a) Example cross-correlation functions, calculated relative to the northwesternmost station on profile L160. (b) Extracted Rayleigh wave phase velocity dispersion curves (Deng *et al.* 2022) used as input for this study. (c) Sensitivity kernel curves for the dispersion curves at different frequency bands. The horizontal axis represents the dimensionless sensitivity, expressed as $(\delta c/c)/(\delta b/b)$, which denotes the normalized partial derivative of phase velocity (c) with respect to S-wave velocity (b).

The Banxi Group is divided into the Ma Diyi Formation and the Woqiangxi Formation from top to bottom. The Ma Diyi Formation is characterized by calcareous muscovite slates and sandstones, which are the primary host rocks for mineralization. The Woqiangxi Formation is composed of quartz sandstones and slates and is oriented east–west.

The Woxi gold mine is located in the central segment of the Xuefeng arcuate structural belt, a key tectonic feature in western Hunan. This belt plays a vital role in controlling mineral deposit distribution, with fault zones like the Xuefeng Fault (F1) having a significant impact. In particular, the Woxi Fault serves as a primary conduit for mineralization, profoundly affecting the geometry and location of the ore bodies (Kuang *et al.* 2004). The ore bodies are predominantly formed as layer veins, filling interlayer fractures and aligning with the surrounding strata. These structural characteristics align with metamorphic hydrothermal mineralization processes (Chen 2018). High-resolution imaging of shallow subsurface structures in this region is critical for resource exploration and ore body identification. In 2019, Deng *et al.* deployed a dense nodal array consisting of 467 SmartSolo seismometers with a central frequency of 5 Hz (Deng *et al.* 2022). The array recorded continuous observations over one month, with seismometers deployed along eight parallel lines, each 10 km long and oriented at an azimuth of 160° (Fig. 8). The average spacing between stations was approximately

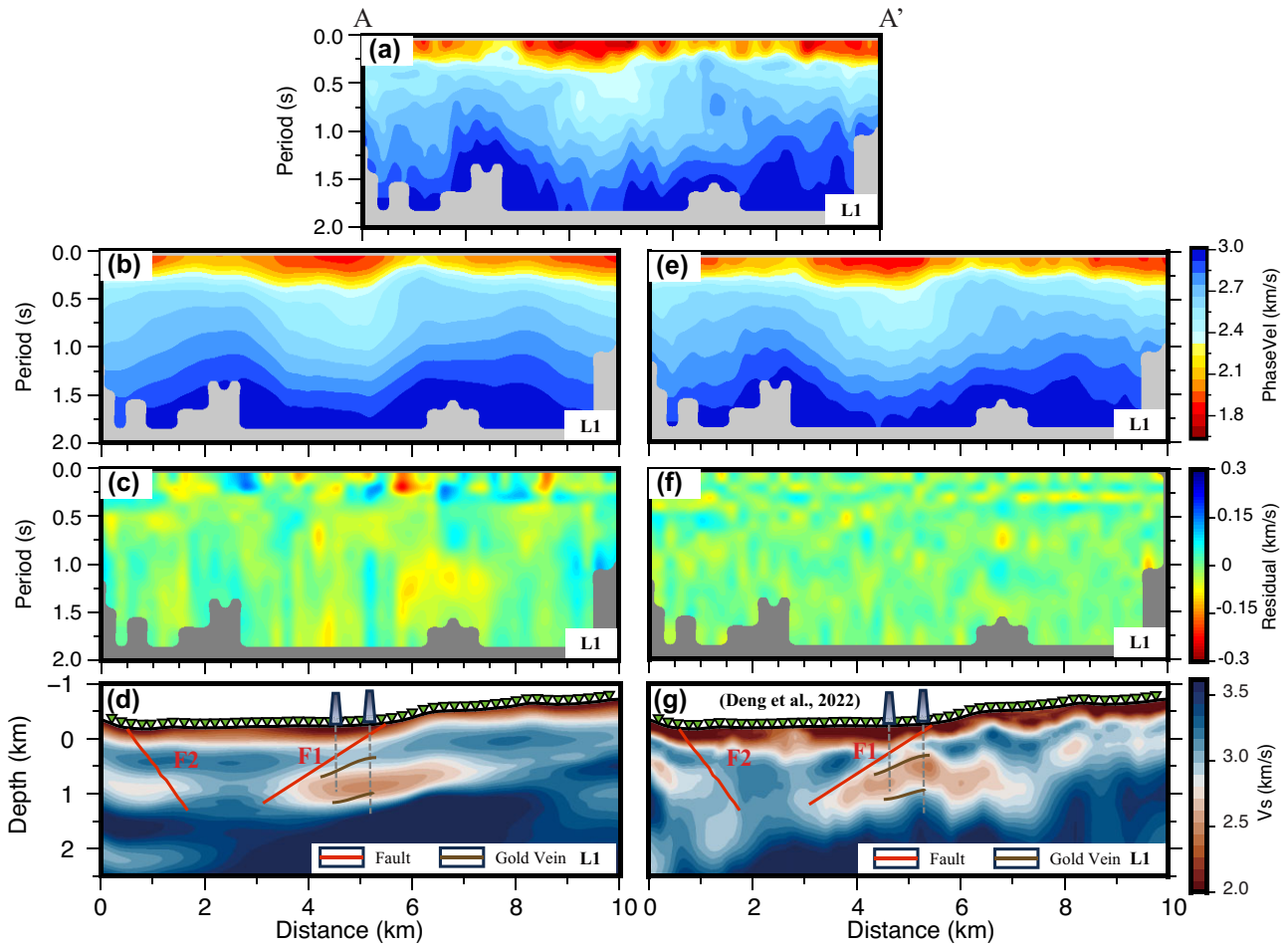

Figure 10. Inversion results and data misfit for the L1 line at the Woxi gold mine. (a) The observed dispersion curves. (b) Predicted dispersion curves from the level-set velocity model (c) Data misfit profile for the level-set method. (d) Velocity model obtained using the level-set method. The red lines indicate the locations of faults, the brown lines mark the verified locations of gold veins. Green triangles represent seismic stations, and the grey trapezoids indicate borehole positions. (e) Predicted dispersion curves from the 1-D inversion model (f) Data misfit profile for the 1-D inversion method. (g) Velocity model obtained from the 1-D inversion method (Deng *et al.* 2022). Other symbols are the same as in (d).

200 m. The final pure-path dispersion curves used in this study (Fig. 9b) were derived following the general workflow of Bensen *et al.* (2007), which involved single-station data pre-processing, cross-correlation of station pairs to compute empirical Green's functions (Fig. 9a), and application of the extended range phase shift method (Deng *et al.* 2022) to extract the final dispersion curves. Additionally, we computed the sensitivity kernel for the dispersion curves (Herrmann 2013) within this frequency band (Fig. 9c). The kernel shows significant sensitivity down to approximately 3 km. The 1-D velocity model employed for this sensitivity calculation was derived from an average velocity model for the area, based on the work of Deng *et al.* (2022).

4.2 Inversion based on the level-set method

The inversion framework used in this study is a geologically guided optimization procedure. Thus, before conducting the level-set inversion, we first analyse the subsurface structures derived from previous 1-D inversion (Deng *et al.* 2022) and the regional geological background (Li *et al.* 2022). Fig. 10(f) shows the inversion results for the L1 profile obtained using the conventional 1-D inversion method. This conventional approach, as thoroughly detailed by Deng *et al.* (2022), systematically inverts broad-band dispersion curves to generate 1-D *S*-wave velocity models beneath each station. As shown in Fig. 10(f), a shallow low-velocity layer, approximately 0.3 km thick with an average velocity of 2.2 km s^{-1}, is distinctly observed. Moreover, between depths of 0.3 and 1 km, a low-velocity body with an approximate velocity of 2.7 km s^{-1} is evident. We also show the fault and mineral vein information derived from the borehole measurements and geological analyses (Deng *et al.* 2022). Overall, the velocity models obtained using the 1-D inversion method show good consistency with the geological structures, particularly in terms of the three-layer stratigraphy. However, some small-scale anomalies are present, likely caused by noise in the dispersion curves (Fig. 10a) and the non-uniqueness of inversion.

We then applied the geological and level-set parametrization method to the dispersion data. The parametrization setup is consistent with that used in the synthetic tests. Given the complexity of fault structures in the region, no fault-related geological information was included in the model definition. Based on the geophysical 1-D inversion results and the

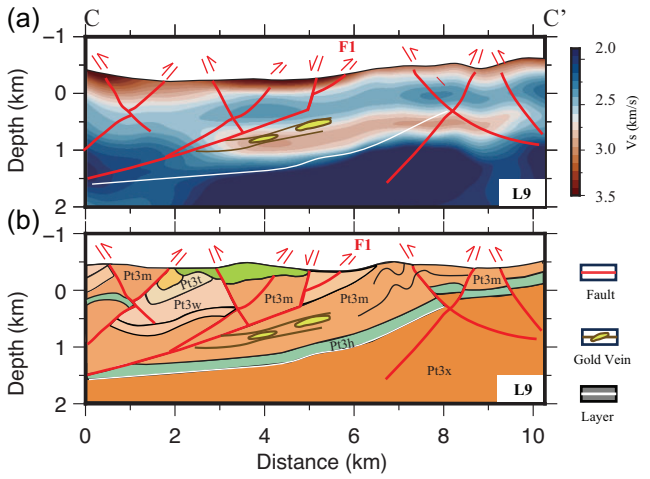

Figure 11. Inversion results of the L9 profile and comparison with the geological cross-section. (a) Inversion results obtained using the Level-set method. The red line indicates the fault location, the brown line represents the vein position and the white lines denote stratigraphic boundaries. (b) Geological cross-section from Li *et al.* (2022) based on geological surveys. The specific stratigraphic interpretations shown here are detailed in the original article by Li *et al.* (2022). For comparative purposes, the major structures identified in (b) are also depicted in (a).

geological context described in Section 4.1, two interfaces were introduced, with average depths of approximately 0.3 and 1.5 km. The model thus has three layers, with average velocities of 2.0, 3.0 and 3.3 km s^{-1}. A 3-D level set was used to define a closed boundary, within which the Gaussian random field had an average velocity of 2.7 km s^{-1}. This initial mean velocity was roughly estimated based on the phase velocities observed in our empirical Green's functions (Fig. 9a) and the results from Deng *et al.* (2022). It is important to note that these parameters were not fixed during the inversion; both the average depths and values of the Gaussian random field were updated iteratively. Tests demonstrated that prior information has minimal influence on the final results. To address the inversion problem, 200 initial model ensembles were used. Each forward simulation was conducted independently, and the inversion process was parallelized to enhance computational efficiency.

Fig. 10 shows the inversion results obtained using the geological and level-set parametrization method. The velocity structure of the L1 profile can be divided into three primary layers. The upper layer, approximately 0.4 km thick, is a low-velocity layer with a velocity of about 2.2 km s^{-1}. The middle layer features alternating low-to-moderate velocities, approximately 2.7 and 3.0 km s^{-1}, corresponding to the Cretaceous strata and the Banxi Group. This layer gradually thins from the northwest to the southeast. The lower layer, at an average depth of around 1 km, is characterized by a moderate-to-high velocity structure, corresponding to the Lengjiaxi Group and underlying granite. This layer rises progressively toward the southeast, becoming shallower. The obtained velocity structure aligns with known geological information, including fault F_1 and the orientations of mineral vein determined from drilling data (Deng *et al.* 2022). In contrast, the model does not clearly resolve the fault F2, an expected outcome as this feature was not explicitly parametrized and is associated with only a weak velocity contrast. Furthermore, the boundary between the deep, high-velocity layers is more distinct, providing clearer insights for geological interpretation.

A comparison between the observed dispersion curves (Fig. 10a) and those predicted by our final models reveals a key difference: the dispersion curve predicted by the model derived with level-set method (Fig. 10b) is very smooth, whereas the prediction from the 1-D inversion method (Fig. 10e) retains strong local fluctuations. We attribute these fluctuations primarily to incoherent noise. As shown in the synthetic tests, the presence of faults and low-velocity bodies does not produce significant variations in the dispersion curves between adjacent stations (Figs 5a and 6a). Sharp local fluctuations similar to those observed in the real data emerge only after incoherent noise is added (Fig. 6b). Therefore, we attribute the strong local variations in the observed dispersion curves are mainly caused by noise. The comparison in Fig. 10 also shows that the level-set method more effectively extracts geologically meaningful and coherent structural information from noisy data.

Using array data for inversion helps suppress incoherent noise, resulting in smoother and more interpretable geological structures. This strategy may lead to some loss of small-scale structural information, but overfitting small-scale disturbances in the data is unnecessary for the region of interest. An alternative approach is to smooth the image after 1-D inversion, but this relies on interpolation algorithms rather than direct data constraints, introducing more subjectivity into the process.

Previous geological studies (Deng *et al.* 2022; Li *et al.* 2022) and the geophysical inversion results suggest that the strike of the gold ore body is in good agreement with the boundary between the low-velocity body and the surrounding high-velocity host rock. Therefore, analysing the boundary of the low-velocity body can provide valuable insights for predicting the strike of an unknown ore body. Due to the inherent non-uniqueness of geophysical inversion and the different data types used, the interface structure obtained by our method differs slightly from previous results (Deng *et al.* 2022). For example, a significant discrepancy is observed in the predicted strike of the ore body at ∼6 km along the profile when comparing results from both methods (Figs 10d and g). Li *et al.* (2022) incorporated regional geological information to develop a geological cross-section, as shown in Fig. 11(b). We plot the velocity profile along the same L9 profile (Fig. 11a), marking the main faults, strata and ore body strikes based on the work of Li *et al.* (2022). Similar to the results for the L1 profile, the geological information in the L9 profile aligns well with the velocity model obtained in this study. Despite minor discrepancies at sharp boundaries, which are expected as both our velocity model (Fig. 11a) and the geological cross-section (Fig. 11b) are interpretations from different data sets, the overall structural trends show strong consistency. Based on this consistency, we infer that the gold ore body likely follows the same structural trend of shallowing to the south and deepening to the north.

To quantitatively assess the uncertainty in the results, we performed inversions using 100 random models and computed the standard deviation of the ensemble of velocity models at each node to estimate the corresponding uncertainty (Fig. 12). Within the depth range of 1 km, the uncertainty is low, whereas the uncertainty increases in the 1–2 km range. This increase is primarily attributed to the inherent decrease in surface wave sensitivity with depth. The frequency band of our dispersion curves (Fig. 9b), which contains limited low-frequency information, further reduces the constraints on deeper structures. As shown in Fig. 12(b), regions with higher uncertainty appear to exhibit a spatial periodicity, which may be linked to the periodic nature of the GRFs. The primary depth range of interest for this gold mine is between 0.5–1 km, where the

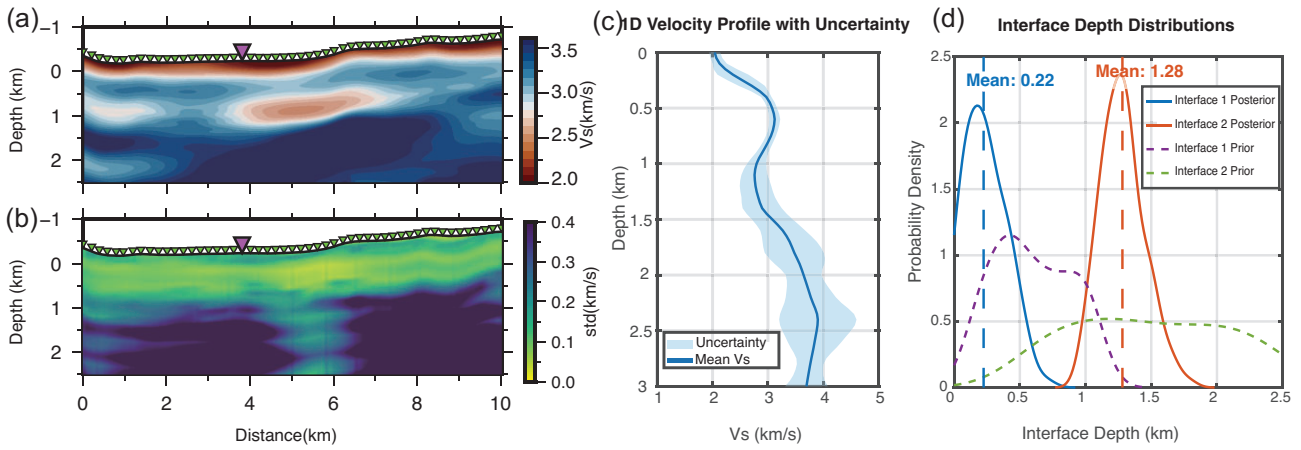

Figure 12. Uncertainty analysis and results for the L1 profile. (a) Velocity profile along the L1 line. Green triangles indicate seismic station locations, and magenta triangles highlight stations from which detailed displays are shown. (b) Uncertainty map along the L1 line, represented by the standard deviation derived from 100 inversion runs. (c) Velocity model and uncertainty (standard deviation) at the magenta station location shown in (a). (d) Estimated depths of the two interfaces at this station. Purple and light green dashed lines represent the prior distributions for the first and second interfaces, respectively. Blue and light brown solid lines show the posterior distributions of interface depths from 100 inversion runs, with their respective means indicated by corresponding vertical lines.

inversion results show stability and relatively high reliability (Fig. 12c). Our method excels at quantitatively determining the position and spatial distribution of subsurface interfaces, demonstrated by the dramatic reduction in uncertainty from the prior to the posterior distributions for the interface depths shown in Fig. 12(d). This capability is crucial for precisely characterizing target interface depths and significantly enhances the exploration of structures of interest. To better constrain areas with higher uncertainty, future work could incorporate additional methods (e.g. receiver function) for joint inversion. This approach could help refine the interface morphology and improve the reliability of the inversion results.

5 DISCUSSION AND CONCLUSION

This study demonstrates that our geology-driven, level-set parametrization offers key advantages over conventional surface wave tomography. Compared to methods reliant on generic grids and generalized smoothness constraints, our approach enables the direct optimization of 3-D interface variations as explicit model parameters. This enhances the recovery of complex interface structures and geometries while avoiding the global smoothing that can obscure geological interpretation. By leveraging level-set functions within an EKI framework, our methodology provides strong lateral continuity between stations, which helps to mitigate incoherent noise and avoid artefacts from artificial regularization, thereby enhancing the objectivity of the results. In practical applications, geological models containing interfaces of interest can be designed based on existing data and preliminary inversion results, allowing for targeted exploration of subsurface structures driven by geological information. This explicit integration of geological models significantly improves the reliability and geological plausibility of the final inversion results. Taken together, both our synthetic tests and real-data application demonstrate that the approach provides an effective imaging method for future seismological studies in the exploration of mineral resources and deposits.

In surface wave tomography, the quality of the seismic data, such as station coverage and the reliability of extracted dispersion curves, is a fundamental factor controlling the final imaging results. In addition, the inversion methodology plays a critical role, as the choice of model parametrization, forward solution approach and inversion algorithm is essential for producing reliable and geologically meaningful imaging results. Different GRFs with varying parameters can lead to significant differences in the inversion of geological body scales. Thus, it is essential to use an appropriate parameter set, such as the characteristic length of the GRFs in inversion. When prior information is available, suitable parameters can be selected through several trial-and-error tests, as demonstrated in this study. A practical strategy is to progressively increase the model's complexity, using the data misfit as a key criterion to test and validate whether each added feature is justified by the data. In cases where prior information is limited, hierarchical generalization of the EKI algorithm can be employed to optimize hyperparameters (Chada *et al.* 2018; Muir *et al.* 2022). Here we also want to note that different forward solution methods do not affect the level-set parametrization or the EKI inversion process. Since the framework treats the forward model as a black box, it is compatible with various types of data inversion or joint inversion. In multidisciplinary inversion, observations from multiple physical fields, such as seismic, electromagnetic and gravity data, can be integrated. The physical properties of the medium can be parametrized in terms of temperature, rock physics properties and composition, while the structural morphology, including strata, tectonic bodies and faults, can also be parametrized. A joint inversion will then provide a more strongly constrained structure. In the future, we will compare two-step tomography using the level-set method with one-step imaging, using a multidimensional parametrization approach combined with forward modelling for multidimensional inversion. Furthermore, the EKI inversion method used in this study can estimate the uncertainty of the results using the statistical properties of the ensemble members. Although this study focuses primarily on optimization, future work could expand on uncertainty estimation to further enhance the reliability of inversion results.

ACKNOWLEDGMENTS

We thank Editor Michal Mlinowski, reviewers Roméo Courbis and Nikita Afonin for their constructive comments and suggestions, which grealy improved the quality of the manuscript. This work was funded by the CAS Project for Young Scientists in Basic Research (grant no. YSBR-082) and the Theory of Hydrocarbon Enrichment under Multi-Spheric Interactions of the Earth (THEMSIE). Maps were created using Generic Mapping Tools (GMT) version 6 (Wessel *et al.* 2019). We also acknowledge the use of the open-source EKI package, available at: https://github.com/jbmuir/EnsembleKalmanInversion.jl, and thank its developers for making this resource available.

DATA AVAILABILITY

The data and invertion code used for the simulation and real data have been permanently archived in the Zenodo repository: https://zenodo.org/records/14886687. The inversion code for the EKI is publicly available on GitHub: https://github.com/jbmuir/EnsembleKalmanInversion.jl. For any inquiries, please contact the corresponding author.

REFERENCES

Aki, K. & Lee, W.H.K. 1976. Determination of three-dimensional velocity anomalies under a seismic array using first P arrival times from local earthquakes: 1. A homogeneous initial model, *J. geophys. Res.,* **81,** 4381–4399.

Aki, K., Christoffersson, A. & Husebye, E.S. 1977. Determination of the three-dimensional seismic structure of the lithosphere, *J. geophys. Res.,* **82,** 277–296.

Aster, R.C., Borchers, B. & Thurber, C.H. 2018. *Parameter Estimation and Inverse Problems,* Elsevier.

Barmin, M.P., Ritzwoller, M.H. & Levshin, A.L. 2001. A fast and reliable method for surface wave tomography, *Pure appl. Geophys.,* **158,** 1351–1375.

Bensen, G. D., Ritzwoller, M. H., Barmin, M. P., Levshin, A. L., Lin, F., Moschetti, M. P., Shapiro, N. M. & Yang, Y., 2007. Processing seismic ambient noise data to obtain reliable broad-band surface wave dispersion measurements, *Geophysical Journal International,* **169,** 1239–1260.

Béreš, M. 2018. Karhunen-Loéve decomposition of isotropic gaussian random fields using a tensor approximation of autocovariance kernel, *High Perform. Comput. Sci. Eng.,* **127,** 188–202.

Boschi, L. & Ekström, G. 2002. New images of the Earth's upper mantle from measurements of surface wave phase velocity anomalies, *J. geophys. Res.: Solid Earth,* **107,** ESE 1–1-ESE 1-14.

Chada, N.K., Iglesias, M.A., Roininen, L. & Stuart, A.M. 2018. Parameterizations for ensemble Kalman inversion, *Inverse Prob.,* **34,** 055009.

Chen, J. 2018. Study on geological characteristics and metallogenic regularity of antimony deposit in Hunan, *West-China Exploration Engineering,* **30,** 123–126

Chmiel, M. *et al.* 2019. Ambient noise multimode Rayleigh and Love wave tomography to determine the shear velocity structure above the Groningen gas field, *Geophys. J. Int.,* **218,** 1781–1795.

Cipta, A., Cummins, P., Dettmer, J., Saygin, E., Irsyam, M., Rudyanto, A. & Murjaya, J. 2018. Seismic velocity structure of the Jakarta Basin, Indonesia, using trans-dimensional bayesian inversion of horizontal-to-vertical spectral ratios, *Geophys. J. Int.,* **215,** 431–449.

Dai, J., Xu, D., Chi, G., Li, Z., Deng, T., Zhang, J. & Li, B. 2022. Origin of the Woxi orogenic Au-Sb-W deposit in the west Jiangnan Orogen of South China: constraints from apatite and wolframite U-Pb dating and pyrite in-situ S-Pb isotopic signatures, *Ore Geol. Rev.,* **150,** 105134.

De La Varga, M., Schaaf, A. & Wellmann, F. 2019. GemPy 1.0: open-source stochastic geological modeling and inversion, *Geosci. Model. Dev.,* **12,** 1–32.

Deng, B., Li, J., Liu, J., Shen, C., Suwen, J. & Chen, Q.-F. 2022. The extended range phase shift method for broadband surface wave dispersion measurement from ambient noise and its application in ore deposit characterization, *Geophysics,* **87,** JM29–JM40.

Du, P. *et al.* 2020. Imaging Karatungk Cu-Ni mine in Xinjiang, Western China with a passive seismic array, *Minerals,* **10,** 601. doi:

Dziewonski, A.M. & Anderson, D.L. 1981. Preliminary reference Earth model, *Phys. Earth planet. Inter.,* **25,** 297–356.

Dziewonski, A.M., Hager, B.H. & O'connell, R.J. 1977. Large-scale heterogeneities in the lower mantle, *J. geophys. Res.,* **82,** 239–255.

Evensen, G. 2012. Sequential data assimilation with a nonlinear quasi-geostrophic model using Monte Carlo methods to forecast error statistics, *J. geophys. Res.: Oceans,* **99,** 10 143–10 162.

Fang, H., Van Der Hilst, R.D., De Hoop, M.V., Kothari, K., Gupta, S. & Dokmanić, I. 2019. Parsimonious seismic tomography with Poisson Voronoi projections: methodology and validation, *Seismol. Res. Lett.,* **91,** 343–355.

Fang, H., Yao, H., Zhang, H., Huang, Y.-C. & Van Der Hilst, R.D. 2015. Direct inversion of surface wave dispersion for three-dimensional shallow crustal structure based on ray tracing: methodology and application, *Geophys. J. Int.,* **201,** 1251–1263.

Feng, M. & An, M. 2010. Lithospheric structure of the Chinese mainland determined from joint inversion of regional and teleseismic Rayleigh-wave group velocities, *J. geophys. Res.: Solid Earth,* **115**.

Gibou, F., Fedkiw, R. & Osher, S. 2018. A review of level-set methods and some recent applications, *J. Comput. Phys.,* **353,** 82–109.

Herrmann, R.B. 2013. Computer Programs in seismology: an evolving tool for instruction and research, *Seismol. Res. Lett.,* **84,** 1081–1088.

Hosseini, K., Sigloch, K., Tsekhmistrenko, M., Zaheri, A., Nissen-Meyer, T. & Igel, H. 2019. Global mantle structure from multifrequency tomography using P, PP and P-diffracted waves, *Geophys. J. Int.,* **220,** 96–141.

Iglesias, M.A. 2015. Iterative regularization for ensemble data assimilation in reservoir models, *Comput. Geosci.,* **19,** 177–212.

Iglesias, M.A. 2016. A regularizing iterative ensemble Kalman method for PDE-constrained inverse problems, *Inverse Prob.,* **32,** 025002.

Isakov, V., Leung, S. & Qian, J. 2015. A fast local level set method for inverse gravimetry, *Commun. Comput. Phys.,* **10,** 1044–1070.

Kovachki, N.B. & Stuart, A.M. 2019. Ensemble Kalman inversion: a derivative-free technique for machine learning tasks, *Inverse Prob.,* **35,** 095005.

Kuang, W., Gu, D. & Liu, X. 2004. Discussion on the mineralization geological features and metallogenetic model of Woxi Au-Sb-W deposit in west Hunan, *Gold,* **25,** 10–15.

Li, B. *et al.* 2022. Structural deformation, metallogenic epoch and genetic mechanism of the Woxi Au-Sb-W deposit, Western Hunan Province, South China, *Sci. China Earth Sci.,* **65,** 2358–2384.

Li, C., Van Der Hilst, R.D., Engdahl, E.R. & Burdick, S. 2008. A new global model for P wave speed variations in Earth's mantle, *Geochem. Geophys. Geosyst.,* **9**.

Li, W. & Qian, J. 2016. Joint inversion of gravity and traveltime data using a level-set-based structural parametrization, *Geophysics,* **81,** G107–G119.

Li, W., Leung, S. & Qian, J. 2014. A level-set adjoint-state method for crosswell transmission-reflection traveltime tomography, *Geophys. J. Int.,* **199,** 348–367.

Li, W., Lu, W., Qian, J. & Li, Y. 2017. A multiple level-set method for 3D inversion of magnetic data, *Geophysics,* **82,** J61–J81.

Lin, F.-C., Li, D., Clayton, R.W. & Hollis, D. 2013. High-resolution 3D shallow crustal structure in Long Beach, California: application of ambient noise tomography on a dense seismic array, *Geophysics,* **78,** Q45–Q56.

Lin, F.-C., Moschetti, M.P. & Ritzwoller, M.H. 2008. Surface wave tomography of the western United States from ambient seismic noise: rayleigh and Love wave phase velocity maps, *Geophys. J. Int.,* **173,** 281–298.

Lin, F.-C., Tsai, V.C. & Schmandt, B. 2014. 3-D crustal structure of the western United States: application of Rayleigh-wave ellipticity extracted from noise cross-correlations, *Geophys. J. Int.,* **198,** 656–670.

Lu, W. & Qian, J. 2015. A local level-set method for 3D inversion of gravity-gradient data, *Geophysics,* **80,** G35–G51.

Montagner, J.P. & Jobert, N. 1988. Vectorial tomography–II. Application to the Indian Ocean, *Geophys. J. Int.,* **94,** 309–344.

Muir, J.B. & Tsai, V.C. 2020. Geometric and level set tomography using ensemble Kalman inversion, *Geophys. J. Int.,* **220,** 967–980.

Muir, J.B., Clayton, R.W., Tsai, V.C. & Brissaud, Q. 2022. Parsimonious velocity inversion applied to the Los Angeles Basin, CA, *J. geophys. Res.: Solid Earth,* **127**.

Nyström, E.J. 1930. Über die praktische auflösung von integralgleichungen mit anwendungen auf randwertaufgaben, *Acta Math.,* **54,** 185–204.

Osher, S. & Sethian, J.A. 1988. Fronts propagating with curvature-dependent speed: algorithms based on Hamilton-Jacobi formulations, *J. Comput. Phys.,* **79,** 12–49.

Peng, J., Hu, R., Zhao, J., Fu, Y. & Lin, Y. 2003. Scheelite Sm-Nd dating and quartz Ar-Ar dating for Woxi Au-Sb-W deposit, western Hunan, *Chin. Sci. Bull.,* **48,** 2640–2646.

Rasmussen, C.E. & Williams, C.K.I. 2005. *Gaussian Processes for Machine Learning (Adaptive Computation and Machine Learning)*. The MIT Press,

Rawlinson, N. & Houseman, G.A. 2010. Inversion for interface structure using teleseismic traveltime residuals, *Geophys. J. Int.,* **708,** 756–772.

Ritzwoller, M.H. & Levshin, A.L. 1998. Eurasian surface wave tomography: group velocities, *J. geophys. Res.: Solid Earth,* **103,** 4839–4878.

Romanowicz, B.A. 2012. Large scale three dimensional P velocity structure beneath the western U.S. and the lost Farallon Plate, *Geophys. Res. Lett.,* **7,** 345–348.

Sambridge, M., Braun, J. & Mcqueen, H. 1995. Geophysical parametrization and interpolation of irregular data using natural neighbours, *Geophys. J. Int.,* **122,** 837–857.

Shearer, P.M. 1991. Constraints on upper mantle discontinuities from observations of long-period reflected and converted phases, *J. geophys. Res.: Solid Earth,* **96,** 18147–18182.

Shen, C. & Liu, J. 2017. *Research Report on the Effectiveness of Comprehensive Geophysical Prospecting Methods for Deep and Edge Prospecting in Non-ferrous (precious) Metal Mines in Hunan Province*. Hunan Non-ferrous Geological Exploration and Research Institute.

Tarantola, A. 2005. *Inverse Problem Theory and Methods for Model Parameter Estimation,* SIAM.

Tsai, V.C., Huber, C. & Dalton, C.A. 2023. Towards the geological parametrization of seismic tomography, *Geophys. J. Int.,* **234,** 1447–1462.

Tso, C.-H.M., Iglesias, M., Wilkinson, P., Kuras, O., Chambers, J. & Binley, A. 2021. Efficient multiscale imaging of subsurface resistivity with uncertainty quantification using ensemble Kalman inversion, *Geophys. J. Int.,* **225,** 887–905.

Wang, X. & Niu, F. 2011. Imaging the mantle transition zone beneath eastern and central China with CEArray receiver functions, *Earthq. Sci.,* **24,** 65–75.

Wessel, P., Luis, J.F., Uieda, L., Scharroo, R., Wobbe, F., Smith, W.H.F. & Tian, D. 2019. The generic mapping tools version 6, *Geochem. Geophys. Geosyst.,* **20,** 5556–5564.

Worthen, J., Stadler, G., Petra, N., Gurnis, M. & Ghattas, O. 2014. Towards adjoint-based inversion for rheological parameters in nonlinear viscous mantle flow, *Phys. Earth planet. Inter.,* **234,** 23–34

Yang, Y., Atterholt, J.W., Shen, Z., Muir, J.B., Williams, E.F. & Zhan, Z. 2021. Sub-kilometer correlation between near-surface structure and ground motion measured with distributed acoustic sensing, *Geophys. Res. Lett.,* **49,** e2021GL096503.

Yao, H., Van Der Hilst, R.D. & De Hoop, M.V. 2006. Surface-wave array tomography in SE Tibet from ambient seismic noise and two-station analysis—I. Phase velocity maps, *Geophys. J. Int.,* **166,** 732–744.

Yao, H., Van Der Hilst, R.D. & Montagner, J.P. 2010. Heterogeneity and anisotropy of the lithosphere of SE Tibet from surface wave array tomography, *J. geophys. Res.: Solid Earth,* **115**.

Yuan, X., Ni, J., Kind, R., Mechie, J. & Sandvol, E. 1997. Lithospheric and upper mantle structure of southern Tibet from a seismological passive source experiment, *J. geophys. Res.: Solid Earth,* **102,** 27 491–27 500.

Zheglova, P., Farquharson, C.G. & Hurich, C.A. 2012. 2-D reconstruction of boundaries with level set inversion of traveltimes, *Geophys. J. Int.,* **192,** 688–698.

Zheglova, P., Lelièvre, P.G. & Farquharson, C.G. 2018. Multiple level-set joint inversion of traveltime and gravity data with application to ore delineation: a synthetic study, *Geophysics,* **83,** R13–R30.

Zheng, T.Y., He, Y.M., Yang, J.H. & Zhao, L. 2015. Seismological constraints on the crustal structures generated by continental rejuvenation in northeastern China, *Sci. Rep.,* **5,** 14995.